

# Rational Design of Biaxial Tensile Strain for Boosting Electronic and Ionic Conductivities of $\text{Na}_2\text{MnSiO}_4$ for Rechargeable Sodium-Ion Batteries

Gamachis Sakata Gurmesa,<sup>[a, d]</sup> Tamiru Teshome,<sup>[e]</sup> Natei Ermias Benti,<sup>[f]</sup>  
Girum Ayalneh Tiruye,<sup>[c]</sup> Ayan Datta,<sup>[g]</sup> Yedilfana Setarge Mekonnen,<sup>\*[b]</sup> and  
Chernet Amente Geffe<sup>\*[a]</sup>

Using first-principles calculations, biaxial tensile ( $\epsilon=2$  and 4%) and compressive ( $\epsilon=-2$  and  $-4\%$ ) straining of  $\text{Na}_2\text{MnSiO}_4$  lattices resulted into radial distance cut offs of 1.65 and 2 Å, respectively, in the first and second nearest neighbors shell from the center. The Si–O and Mn–O bonds with prominent probability density peaks validated structural stability. Wide-band gap of 2.35 ( $\epsilon=0\%$ ) and 2.54 eV ( $\epsilon=-4\%$ ), and narrow bandgap of 2.24 eV ( $\epsilon=+4\%$ ) estimated with stronger

coupling of p–d  $\sigma$  bond than that of the p–d  $\pi$  bond, mainly contributed from the oxygen p-state and manganese d-state.  $\text{Na}^+$ -ion diffusivity was found to be enhanced by three orders of magnitude as the applied biaxial strain changed from compressive to tensile. According to the findings, the rational design of biaxial strain would improve the ionic and electronic conductivity of  $\text{Na}_2\text{MnSiO}_4$  cathode materials for advanced rechargeable sodium-ion batteries.

## Introduction

State-of-the-art rechargeable batteries, most commonly, lithium-ion and sodium-ion batteries have brought growing interest for a vast range of applications. For instance, rechargeable lithium-ion batteries (LIBs) are widely used from small appliances (smartphones, laptops, headphones, etc.) to large systems including sustainable transportations (electric vehicles, hybrid- and plug-in hybrid vehicles, etc.) and uninterruptible power supply. However, the abundance of Na metal and its affordable cost, for large-scale applications compared to LIBs

are paving the way for the development of rechargeable sodium-ion batteries (SIBs).<sup>[1–4]</sup>

Recently, SIBs have attracted growing interest and are becoming among the most contemporary research topics due to their rocking chair storage mechanism compared to LIBs. For the development of SIBs, sodium layered transition metal oxides have been rationally designed and used as electrode materials. For instance, the combination of Na with other metal oxides ( $\text{NaMO}_2$ ,  $M=\text{Ni}$ ,  $\text{Mn}$ ,  $\text{Fe}$ ) have been observed as cathode material for promising electrochemical performance.<sup>[5–7]</sup> In addition, the symmetric  $\text{LiNi}_{1/3}\text{Mn}_{1/3}\text{Co}_{1/3}\text{O}_2$  (NMC) compound was presented [8] as a 4 V cathode material to replace  $\text{LiCoO}_2$ ,

[a] G. Sakata Gurmesa, Dr. C. Amente Geffe  
Department of Physics  
College of Natural and Computational Sciences  
Addis Ababa University  
P. O. Box 1176,  
Addis Ababa (Ethiopia)  
E-mail: chernet.amente@aau.edu.et

[b] Dr. Y. Setarge Mekonnen  
Center for Environmental Science  
College of Natural and Computational Sciences  
Addis Ababa University  
P. O. Box 1176,  
Addis Ababa (Ethiopia)  
E-mail: yedilfana.setarge@aau.edu.et

[c] Dr. G. Ayalneh Tiruye  
Materials Science Program/Department of Chemistry  
College of Natural and Computational Sciences  
Addis Ababa University  
P. O. Box 1176,  
Addis Ababa (Ethiopia)

[d] G. Sakata Gurmesa  
Department of Physics  
College of Natural and Computational Sciences  
Addis Ababa University  
P. O. Box 318,  
Mettu (Ethiopia)

[e] Dr. T. Teshome  
Department of Physics  
College of Natural and Social Sciences  
Addis Ababa Science and Technology University  
P. O. Box 16417  
Addis Ababa (Ethiopia)

[f] Dr. N. Ermias Benti  
Department of Physics  
College of Natural and Computational Sciences  
Wolaita Sodo University  
P. O. Box 138  
Wolaita Sodo (Ethiopia)

[g] Prof. Dr. A. Datta  
School of Chemical Sciences  
Indian Association for the Cultivation of Science  
2A and 2B, Raja S. C. Mullick Road  
Jadavpur, Kolkata 700032, West Bengal (India)

 Supporting information for this article is available on the WWW under <https://doi.org/10.1002/open.202100289>

 © 2022 The Authors. Published by Wiley-VCH GmbH. This is an open access article under the terms of the Creative Commons Attribution Non-Commercial License, which permits use, distribution and reproduction in any medium, provided the original work is properly cited and is not used for commercial purposes.

with significantly greater voltage, superior structural stability, and safety even at extreme temperatures, as well as higher reversible charge capacity.<sup>[8–10]</sup> The reversible specific capacity of NMC was measured to be as low as 160 mAhg<sup>-1</sup> in the cut-off potential range of 2.5–4.4 V and 200 mAhg<sup>-1</sup> in that of 2.8–4.6 V.<sup>[11]</sup>

Because of their superior thermal stability and strong bonds between transitional metals and ligands, polyanion-based transition metal oxide electrode materials are found to be more appealing than those of the layered family. For instance, composite of sodium and transition metals containing polyanion compounds, NaMPO<sub>4</sub> (M=Mn, Fe, Co, and Ni), are excellent electrode materials for hybrid supercapacitors<sup>[12,13]</sup> with the capacity in the range of 160–250 Fg<sup>-1</sup>. However, AMPO<sub>4</sub> (A=Li, Na; M=Mn, Fe, Co, and Ni) based electrode materials<sup>[12–16]</sup> have a unidirectional ionic diffusion, which may limit the capacitive performance of energy storage devices. As a result, di-sodium (lithium)-ion transition metal orthosilicates, A<sub>2</sub>MSiO<sub>4</sub> (A=Li, Na; M=Mn, Fe, Co, and Ni) electrode materials have emerged as a viable alternative, allowing for two-electron redox processes with higher capacity of more than 330 mAhg<sup>-1</sup>.<sup>[17–21]</sup> Furthermore, di-sodium-based orthosilicate compounds are a good candidate for electrode materials due to their low cost, high thermal stability, and non-toxicity in addition to the high abundance of silicon, sodium, and manganese in the earth's crust.<sup>[21–23]</sup>

Experimentally, di-sodium based orthosilicate compounds (Na<sub>2</sub>MSiO<sub>4</sub>, M=Mn, Fe, Co, and Ni) can be successfully synthesized for SIBs via different methods such as modified two-step route,<sup>[24]</sup> electrochemical Li–Na ion-exchange,<sup>[21]</sup> sol-gel method,<sup>[25]</sup> and the solid-state reaction of Na<sub>2</sub>CO<sub>3</sub>, MnCO<sub>3</sub>, and SiO<sub>2</sub>.<sup>[26]</sup>

Previous computational studies based on ab initio molecular dynamics (AIMD), density functional theory with (out) Hubbard-correction (DFT, DFT+U), and classical molecular dynamics simulation (CMD) have demonstrated the structural stabilities, electronic structures, and electrochemical properties of materials.<sup>[27–32]</sup> For example, DFT and DFT+U study of di-sodium orthosilicate compounds indicates that Na<sub>2</sub>MSiO<sub>4</sub> (M=Mn, Fe, Co, Ni) with Pc-symmetry has better structural stability and faster ionic conductivity than lithium orthosilicate. This is due to the wider distance between atomic layers and non-directional bonding between Na and neighboring atoms, indicating di-sodium orthosilicate electrode materials' potential suitability for SIBs. Another DFT calculation also revealed that the Na<sup>+</sup> ion in Na<sub>2</sub>MnSiO<sub>4</sub> migrates quickly through 3D diffusion channels and has a lower activation barrier than the Li<sup>+</sup> ion in Li<sub>2</sub>MnSiO<sub>4</sub>.<sup>[33]</sup>

## Crystal Structures and Computational Method

The Na<sub>2</sub>MSiO<sub>4</sub> family crystallizes in a monoclinic crystal system with *Pn* or *Pc* symmetry,<sup>[27,28,30–34]</sup> whereas Li<sub>2</sub>MSiO<sub>4</sub> crystallizes in an orthorhombic system with *Pmn*2<sub>1</sub> symmetry.<sup>[34–36]</sup> The lattice parameters for monoclinic Na<sub>2</sub>MnSiO<sub>4</sub> with *Pn* symmetry

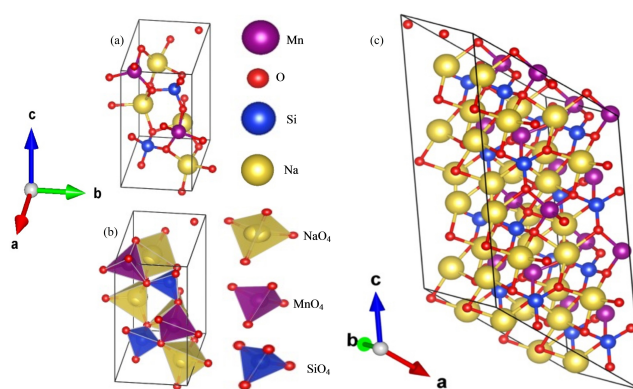
computed by Nalbandyan and coworkers are  $a = 7.02857$ ,  $b = 5.60957$ ,  $c = 5.33391$ ,  $\beta = 90.0^\circ$ ,  $\alpha = 89.7949^\circ$ , and  $\gamma = 90^\circ$ .<sup>[37]</sup>

Figure 1 depicts the crystal structure of Na<sub>2</sub>MnSiO<sub>4</sub> based on the iso-structural Na<sub>2</sub>ZnSiO<sub>4</sub>, which was obtained from the materials project.<sup>[38]</sup> The crystal structure of Na<sub>2</sub>MnSiO<sub>4</sub> is shown in the DFT-optimized unit cell (Sch. 1 (a and b)) and supercell (Sch. 1c). According to the Jahn-Teller effect, Mn–O bonding (MnO<sub>4</sub>) distortion is greater than Na–O (NaO<sub>4</sub>) and Si–O (SiO<sub>4</sub>), which form corner-sharing tetrahedral units with four oxygen atoms and have a similar tendency to Li<sub>2</sub>MnSiO<sub>4</sub>.<sup>[39–41]</sup>

However, in polyanion-type cathode materials based on XO<sub>4</sub> (X=P, Si, S, and so on) groups,<sup>[42–46]</sup> oxygen atoms are linked by strong covalent bonds, which could limit oxygen evolution. Polyanion-type cathodes are therefore more thermally stable than layered transition metal oxides, ensuring greater safety in large-scale applications. Na<sub>2</sub>MnSiO<sub>4</sub> has superior thermal stability due to the strong bond between Si and O in the complex structure of the SiO<sub>4</sub> tetrahedral unit.

The biaxial strain engineering was implemented using equation  $\varepsilon = \Delta a/a_0$  where  $\varepsilon$  is strain ratio,  $a_0$  is the equilibrium lattice, and  $\Delta a \pm a_0$  is tensile or compressive strain. The calculations were carried out in the framework of DFT<sup>[47,48]</sup> using both the Grid-based projector augmented wave method (GPAW)<sup>[49]</sup> and Vienna ab initio Software Package (VASP).<sup>[50]</sup> The exchange and correlations functional were examined with generalized gradient approximations (GGA) by the Perdew–Burke–Ernzerhof (PBE) functional.<sup>[51]</sup> The core ions and valence electrons interactions were treated by the projected-augmented wave (PAW)<sup>[52]</sup> potential. All the structural relaxations were performed with a 4×4×3 and 2×2×2 k-point Monkhorst–Pack grid, respectively, for a unit cell and supercell as shown in Figure 1.

To treat the electron correlation of the localized d electronic states, the simplified approach to the DFT+U theory introduced by Dudarev et al.<sup>[53]</sup> was applied as implemented in both GPAW and VASP codes. The electron self-interaction error (SIE) with GGA (PBE) functional were managed by adjusting the Hubbard coefficient<sup>[54]</sup> correction for Mn (3d) in the case of Na<sub>2</sub>MnSiO<sub>4</sub>. In this study, the Hubbard (U) correction values of



**Figure 1.** DFT-optimized unit cell of Na<sub>2</sub>MnSiO<sub>4</sub> crystal structure (a) the unit cell with ball and stick model, (b) the unit cell with tetrahedral complexes of MnO<sub>4</sub>, SiO<sub>4</sub>, NaO<sub>4</sub>, and (c) the supercell constructed from 2×2×2 repetition.

$U = 3.9$  eV (VASP) and  $1.5$  eV (GPAW) were used for Mn in  $\text{Na}_2\text{MnSiO}_4$ .

The structural stability of  $\text{Na}_2\text{MnSiO}_4$  supercell at room temperature ( $T = 300$  K) was validated by performing AIMD simulations, as previously reported.<sup>[55–57]</sup> The AIMD simulations were done using the VASP package for 10 ps with a time step of 0.5 fs. The energy barrier ( $E_b$ ) of various sodium diffusion pathways was calculated using the climbing-image nudged elastic band (CI-NEB) method<sup>[58–60]</sup> using GPAW code. Five intermediate images were adjusted to interpolate the initial and final states along with the  $\text{Na}^+$ -ion diffusion path. Furthermore, the following Arrhenius equation was used to calculate the  $\text{Na}^+$ -ion diffusion rate ( $r$ ) and  $\text{Na}^+$ -ion diffusion coefficient ( $D$ ).

$$D = a^2 r \quad (1)$$

$$r = \nu e^{-E_b/k_B T} \quad (2)$$

where,  $a$  is the minimum jump length of the Na atom from one site to another by following the possible channel,  $r$  is diffusion rate,  $E_b$  is energy barrier,  $e$  is the electronic charge,  $\nu = 10^{13} \text{ s}^{-1}$  is the hopping rate,  $k_B = 8.6173326 \text{ eV K}^{-1}$ , is the Boltzmann constant, and  $T = 300$  K is the temperature.

## Results and Discussion

In this section, structural analysis, electronic structures,  $\text{Na}^+$ -ion diffusions in (un)strained  $\text{Na}_2\text{MnSiO}_4$  are explained in more detail.

### Structural Analysis

We will use the radial distribution functions (RDFs or  $g(r)$ ), partial RDFs ( $g_{i-j}(r)$ ), bond angle distribution functions (BADFs or  $B(r)$ ), partial BADFs ( $B_{i-j}(\theta)$ ) for O–Si–O and O–Mn–O, bond length distribution functions (BLDFs or  $B(r)$ ), and partial BLDFs ( $B_{i-j}(r)$ ) to describe biaxial strained  $\text{Na}_2\text{MnSiO}_4$  lattice.

### Radial Distribution Functions (RDFs)

Radial distribution functions (RDFs) represent the spatial organization of ions around a central ion and are often employed in simulations. They can also be derived indirectly from X-ray spectra.

Molecules fluctuate near their lattice sites in solids, which have regular, periodic shapes. Because the structure is extremely long-range, defects in solids are uncommon. There is no likelihood of finding a particle between their peaks because all molecules are packed consistently to occupy the area most efficiently. Each peak symbolizes a solid's coordination shell, with the closest neighbors in the first shell, the second in the second, and so on.

RDFs is the probability density of finding an atom at a randomly chosen point at a distance  $r$  from a central atom,

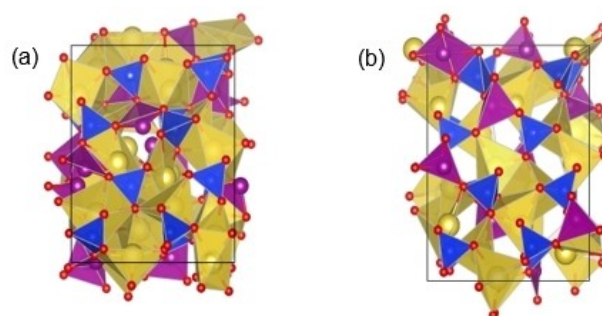
divided by the mean number density. Hence, radial distribution function (RDF) is defined by  $g(r) = n(r)/4\pi r^2 \Delta\rho_o$ , where  $n(r)$  fluctuates around but on average approaches  $4\pi r^2 \rho_o$  at large  $r$ , where  $\rho_o$  is the mean number density.

Moreover, partial radial distribution function (PRDF) is defined by  $g_{i-j}(r) = n_{ij}(r)/\rho_{i-j} 4\pi r^2 \Delta r_{ij}$ , where  $n_{ij}(r)$  is the number of  $j$ -atoms within a distance  $[r + \Delta r_{ij}]$  from an  $i$  atom and  $\rho_{i-j} = \sqrt{\rho_i \rho_j}$ , where  $\rho_i$  and  $\rho_j$  are number densities of the two species. The height of the first peak in  $g_{i-j}(r)$  represents the relative probability of finding  $j$ -atoms in the first shell of an  $i$ -atom.

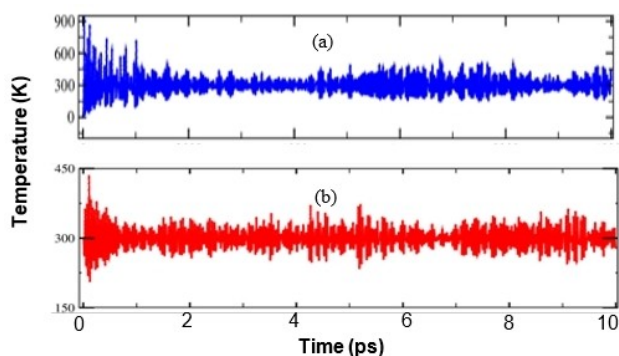
The AIMD simulations were performed to confirm the thermal stability of  $\text{Na}_2\text{MnSiO}_4$  crystal structure modified by biaxial tensile strain at  $\varepsilon = 4\%$  (Figure 2a) and compressive strain at  $\varepsilon = -4\%$  (Figure 2b). Figure 3 shows the temperature versus time graph, indicating that the average temperature fluctuations are 318.45 K and 329.35 K, respectively at  $T = 300$  K. The positional fluctuation of each atom equilibrates within a few ps, indicating dynamic stability with no structural degradation.

Figure 4 show the radial distribution functions,  $g(r)$ , for the probability density of the first (1.65 Å) and second (2.0 Å) NN shells from the center. The sharpness of the first and second peaks reflect the system's crystalline structure, whereas the  $g(r)$  profile reveals the most contributing atom to the system.

Figure 5 summarized the average bond length distributions calculated for Si–O (1.653 Å at  $\varepsilon = 4$  and  $-4\%$ ) and Mn–O



**Figure 2.** Biaxial strain of (a)  $\varepsilon = 4\%$  and (b)  $\varepsilon = -4\%$  applied to the  $\text{Na}_2\text{MnSiO}_4$  crystal structure.



**Figure 3.** Temperature fluctuation about 300 K using AIMD simulation as a function of (a)  $\varepsilon = 4\%$  and (b)  $\varepsilon = -4\%$  (b).

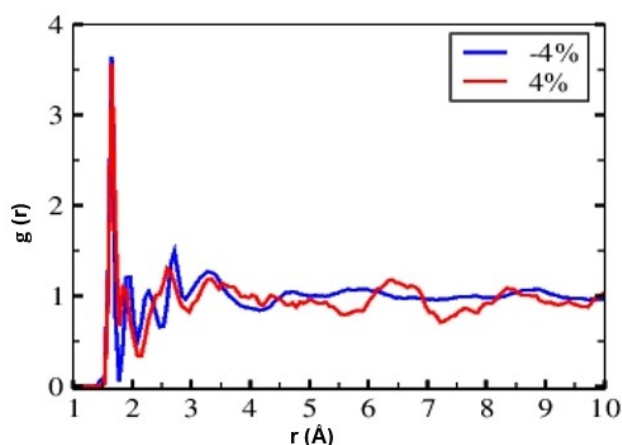


**Figure 4.** Temperature fluctuation about 300 K using an AIMD simulation (a) at  $\varepsilon = -4\%$  and (b)  $\varepsilon = 4\%$  (b).

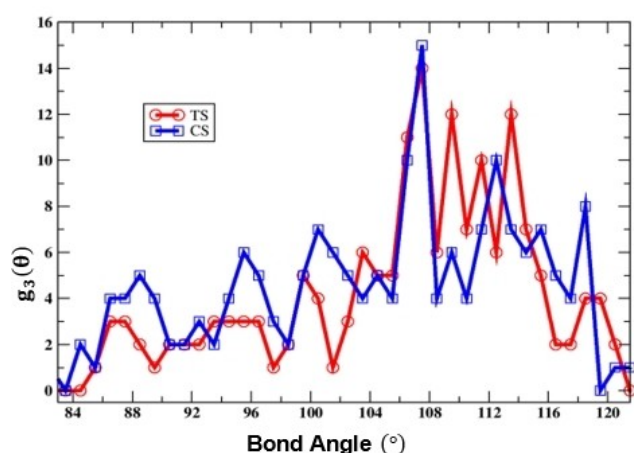


**Figure 5.** Total bond angle distribution function ( $g_3(\theta)$ ) at  $\varepsilon = -4\%$  (blue),  $\varepsilon = 4\%$  (red) using AIMD simulation.

(1.876 Å at  $\varepsilon = 4\%$  and 1.932 Å at  $\varepsilon = -4\%$ ), respectively, for the first and second NN shell. For Si–O bonding, there is no structural change, but there is a slight change in the local environment around Mn–O bonding that does not cause significant  $\text{Na}_2\text{MnSiO}_4$  lattice distortion.

The biaxially strained  $\text{Na}_2\text{MnSiO}_4$  lattice maintains structural stability without major lattice distortions. For example, while the probability density of Si–O bonding pair atoms with biaxial tensile strain (red) is slightly lower than that of compressive strain (blue), both are visible at the first NN ( $\approx 1.65$ ) from the center.

This shows that, unlike Mn–O bonding, where the biaxial tensile (magenta) is somewhat greater than the biaxial compressive (green) strain at the second NN (2.0 Å), the strong Si–O bond plays a critical role in maintaining the structural stability of the system. These graphs show a series of well-defined peaks matching to successive nearest-neighbor distances, as would be expected from an ordered solid at room temperature. However, there is no significant change in peak position for the Si–O and Mn–O couples. There are no notable

peaks beyond 2.2, which is consistent with experimental observations.<sup>[61–63]</sup>

### Bond Angle Distribution Function

Local information about local symmetry can be obtained from bond angle distribution functions. It's a triplet correlation inside the cut off distance, which is defined for angles between atoms surrounding the core atom's nearest neighbors. The cut off distance, which is the initial minimal location of  $g(r)$ , is used to generate bond-angle distribution as a function of biaxial strain, as shown in Figures 5 and 6. Figure 5 shows the total bond angle distribution as a function of biaxial strain, while Figure 6 depicts the angular correlation function for O–Si–O and O–Mn–O under biaxial tensile and compressive strain. Under applied biaxial strain, the estimated bond-angle distribution of  $\text{Na}_2\text{MnSiO}_4$  revealed notable peaks at  $90^\circ$  and  $109^\circ$ . Furthermore, Figure 6 shows that for both biaxial tensile and compressive strain, the notable peaks at  $90^\circ$  are contributed by the O–Mn–O angle, while those at  $109^\circ$  are contributed by the O–Si–O angle, in keeping with earlier theoretical and experimental findings.<sup>[28,64,65]</sup>

### Bond Length Distribution Function

As shown in Figure 7, bond length distribution analysis was utilized to assess the bond strength of the system subjected to biaxial strain. It shows that the total bond length exhibits prominent maxima for the first and second NN shells at radial distances of 1.65 and 2.00 Å, respectively, with the same pattern as  $g(r)$ .

Furthermore, the partial bond angle distribution functions revealed that the Si–O and Mn–O bonding, respectively, contributed primarily to the total bond angles distribution functions within the first and second NN shells, with little variation when biaxial strain was applied (Figure 8). The

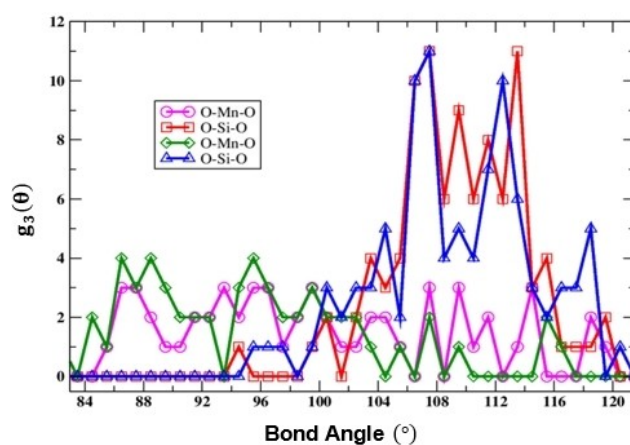


**Figure 6.** Partial bond angle distribution function ( $g_3(\theta)$ ) profile as a function of bond angle at 300 K;  $\varepsilon = 4\%$  for O–Mn–O (magenta) and O–Si–O (red),  $\varepsilon = -4\%$  for O–Mn–O (green) and O–Si–O (blue) using AIMD simulation.

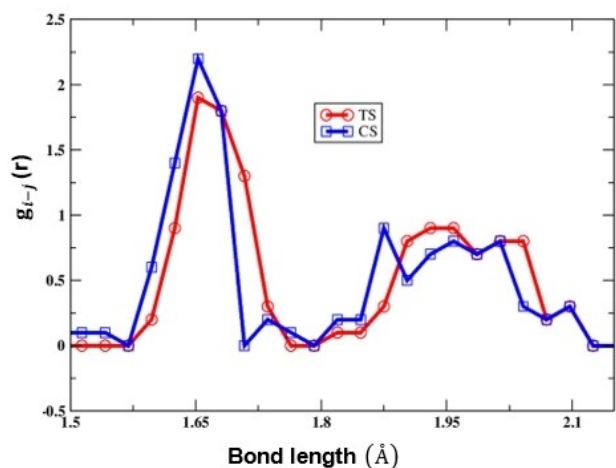


**Figure 7.** Total bond-length distribution function ( $g_{i-j}(r)$ ) profile as a function of bond-length at  $\varepsilon = -4\%$  (blue),  $\varepsilon = -4\%$  (red) using AIMD simulation at 300 K.

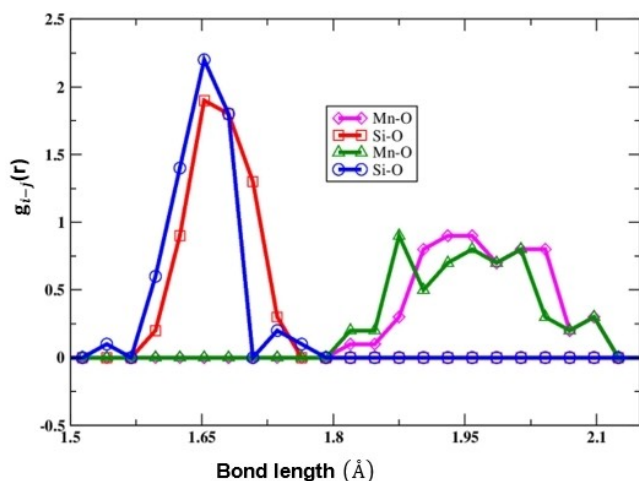


**Figure 8.** Partial bond-length distribution function ( $g_{i-j}(r)$ ) profile as a function of bond length at  $\varepsilon = 4\%$  for Mn–O (magenta) and Si–O (red),  $\varepsilon = -4\%$  for Mn–O (green), and Si–O (blue).

computed bond angles and bond length in this study accord well with previous theoretical and experimental work,<sup>[28,61–64]</sup> indicating that the crystal structure of  $\text{Na}_2\text{MnSiO}_4$  is stable.

### Electronic Structures

The charge-discharge kinetics, which is mediated by charge carriers including electrons, ions, and/or polarons, have significant potential to determine the conductivity, and thus, the rate performance of the battery cell. The conductivity of orthosilicate  $\text{A}_2\text{MnSiO}_4$  ( $\text{A}=\text{Li}, \text{Na}$ ) cathode materials that have been so far investigated via both experiment and computation methods proved very poor intrinsic ionic and electronic conductivity.<sup>[11,13]</sup> The electronic structures of  $\text{Na}_2\text{MnSiO}_4$ , such as projected density of states (PDOS) and band structures, were investigated

using DFT and DFT+U methods applied in the GPAW and VASP codes.

The delocalization problem in the 3d-orbitals of the Mn atom in  $\text{Na}_2\text{MnSiO}_4$  was solved using the DFT+U approach following the previous studies.<sup>[29,30]</sup> Despite the fact that determining the correct U-value is a difficult task, Table 1 displays the computed  $E_g$  with several U-values ranging from 1 to 6 eV with 0.5 intervals, with the U-value of 1.5 eV ( $E_g = 2.35$  eV) being fixed for further analysis.<sup>[29]</sup>

To our knowledge, this is the first calculated bandgap for  $\text{Na}_2\text{MnSiO}_4$  using the GPAW method, and it agrees well with the bandgap of 2.35 eV estimated by the VASP code (for  $U = 3.9$  eV). Furthermore, it agrees with Bianchini and coworkers,<sup>[70]</sup> who predicted the bandgap of  $\text{Na}_2\text{MnSiO}_4$  material to be 2.37, 1.23, 3.02, and 2.44 eV for  $M=\text{Mn}, \text{Fe}, \text{Co},$  and  $\text{Ni}$ , respectively. Figure 9 presented the electronic projected density of states (also mentioned in Figure S1, Supporting Information) and their related band structures analysis, demonstrating electron transfer to each orbital in the constituent elements of  $\text{Na}_2\text{MnSiO}_4$  before biaxial strain was applied. To the best of our knowledge, this is the first  $E_g$  value calculated for  $\text{Na}_2\text{MnSiO}_4$  using the GPAW code which is in good agreement with the bandgap calculated using the VASP code of 2.35 eV (at  $U = 3.9$  eV).

Moreover, it also matches well with the work of Bianchini and coworkers<sup>[70]</sup> who calculated the bandgap of  $\text{Na}_2\text{MnSiO}_4$  material to be 2.37, 1.23, 3.02, and 2.44 eV, respectively, for  $M=\text{Mn}, \text{Fe}, \text{Co},$  and  $\text{Ni}$ . DFT calculations revealed the electronic projected density of states (Figure 10 and Figure S1, Supporting Information), while the band structures analysis (Figure 11), confirming electron transfer to each orbital in the constituent elements of  $\text{Na}_2\text{MnSiO}_4$  material before applying biaxial strain.

**Table 1.** Calculated  $E_g$  values as a function of Hubbard (U) correction (eV) for unstrained  $\text{Na}_2\text{MnSiO}_4$ .

U[eV]	0	1.5	2.5	3.5	4.5	5.5
$E_g$ [eV]	1.84	2.35	2.64	2.88	3.09	3.25

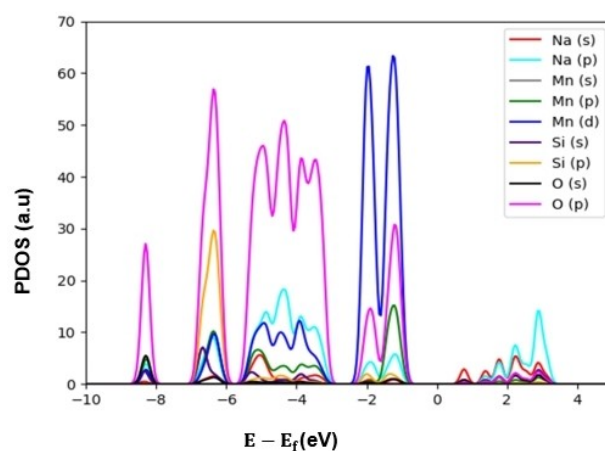


**Figure 9.** Calculated projected density of state (PDOS) using the PBE functional.

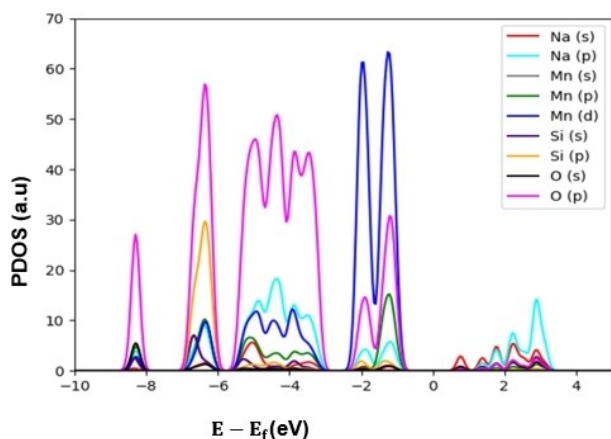


Figure 10. Calculated projected density of state (PDOS) using PBE+U ( $U=1.5$  eV) functional.

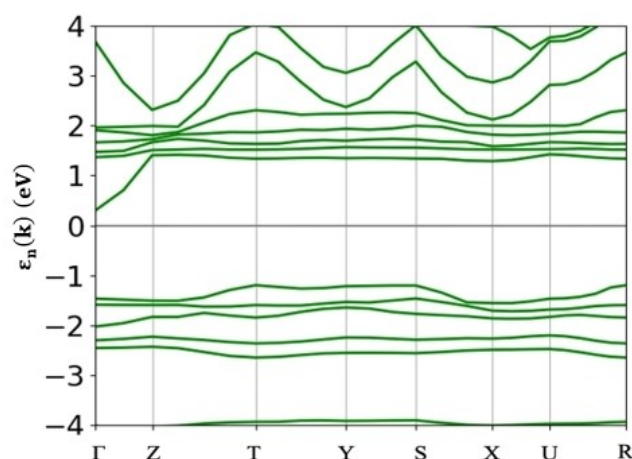


Figure 12. Calculated band structure using PBE+U ( $U=1.5$  eV) functional.

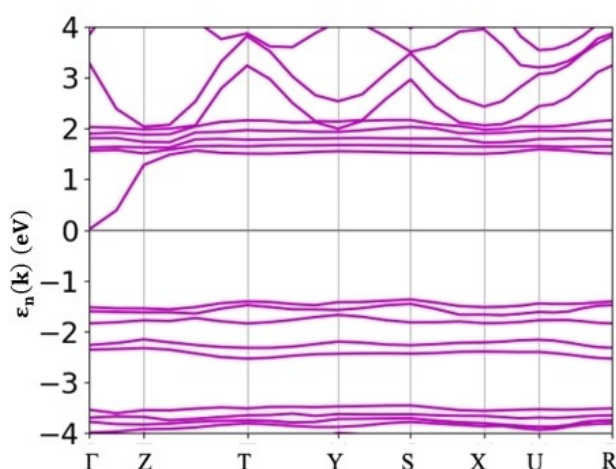


Figure 11. Calculated band structure using the PBE functional.

Furthermore, around the Fermi level from the valence band region, the spectrum of the Mn (d) orbital calculated using the PBE functional was shown to be more dominating than that of the O (p) orbital.

The PBE+U results (Figures 10 and 12), on the other hand, revealed that the spectrum of the O(p) orbital becomes more prominent. This finding showed a similar tendency in our prior research for  $\text{Li}_2\text{MnSiO}_4$  material.<sup>[29]</sup> When comparing the PBE-based predicted bandgap of 1.84 eV (Figures 9 and 11) to the PBE+U-determined bandgap of 2.35 eV (Figures 10 and 12). The estimated value of the bandgap of bulk  $\text{Na}_2\text{SiO}_4$  from the ordinary PBE-based PDOS and the corresponding band structure was lower by about half eV relative to the PBE+U results.

The partial charge density for the valence band maximum (VBM) and conduction band minimum (CBM) were presented in Figures 13a and b, suggesting that the orbital orientation aligned in the p-d coupling or hybridization is in good agreement with the PDOS exhibited in Figures 9 and 10.

According to DFT+U (at  $U=1.5$  eV) calculations, the total magnetic moments of  $\text{Na}_2\text{MnSiO}_4$  estimated to be 4 (at  $\epsilon=0\%$ ),

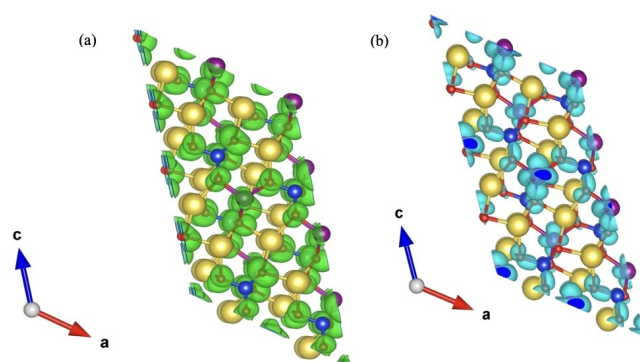


Figure 13. Partial charge density (a) VBM and (b) CBM calculated by PBE functional.

4.1 (at  $\epsilon=-4\%$ ), and 3.9 ( $\epsilon=+4\%$ ). The average magnetic moments for the Mn ion before and after biaxial strain were found to be 4.51 (at  $\epsilon=+4\%$ ), 4.50 (at  $\epsilon=+2\%$ ), 4.49 ( $\epsilon=0\%$ ), 4.47 (at  $\epsilon=-2\%$ ), and 4.46 (at  $\epsilon=-4\%$ ), respectively. The comprehensive study of the magnetism, electronic, and atomic structure can help to better understanding the fundamentals of metal-ion battery materials.<sup>[71,72]</sup>

Figure 14 summarizes the effect of biaxial straining on the bandgap ( $E_g$ ) and activation energy barrier ( $E_b$ ) of  $\text{Na}_2\text{MnSiO}_4$  computed using the PBE ( $E_{g1}$ ) and PBE+U ( $E_{g2}$ ) functionals. The figure furthermore details how biaxial strain (tensile and compression) affects the electronic and ionic conductivities of  $\text{Na}_2\text{MnSiO}_4$ . It could be deduced that biaxial tensile straining (at  $\epsilon=4\%$  and  $2\%$ ) resulted in a smaller bandgap and lower energy barrier than biaxial compressive straining (at  $\epsilon=-4\%$  and  $-2\%$ ). It should be noted that the biaxial tensile strained  $\text{Na}_2\text{MnSiO}_4$  is semiconductor-like and has improved  $\text{Na}^+$  ion conductivity.

Moreover, the energy minimization, volume, energy barriers, and the total density of states as a function of biaxial strain ( $-4$ ,  $-2$ ,  $0$ ,  $2$ , and  $4\%$ ) were summarized in Figures S2–S5 (Supporting Information). We presented a tight-binding model of the  $s$ ,  $p_x$ ,  $p_y$ , and  $d$  orbitals to comprehend this mechanism, i.e., the

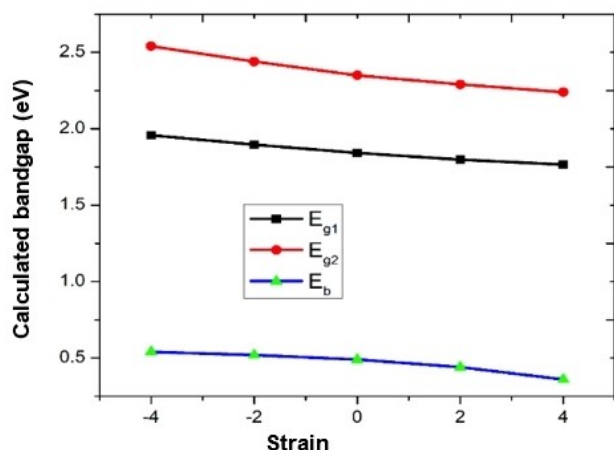


Figure 14. Calculated bandgap as a function of biaxial strain.

logic behind the band increase and/or decrease. To this, the effective Hamiltonian is considered as Equation (3):

$$H_{TB} = \sum_{i,\alpha} \varepsilon_i^\alpha c_i^{\alpha+} c_i^\alpha + \sum_{(i,j),\alpha,\beta} t_{ij}^{\alpha\beta} (c_i^{\alpha+} c_j^\beta + h.c.). \quad (3)$$

Here  $\varepsilon_i^\alpha$ ,  $c_i^{\alpha+}$  and  $c_i^\alpha$  represent the on-site energy, creation, and annihilation operators of an electron at the  $\alpha$ -orbital of the  $i^{\text{th}}$  atom. The parameter  $t_{ij}^{\alpha\beta}$  is the nearest-neighbor hopping energy of an electron between the  $\alpha$ -orbital of the  $i^{\text{th}}$  atom and the  $\beta$ -orbital of the  $j^{\text{th}}$  atom,  $\alpha, \beta \in (p_x, p_y, p_z, d)$ , which can be calculated from the on-site energies of  $s$ ,  $p$ , and  $d$  orbitals by setting the values of  $\varepsilon_{Na}^s = -5.13$  eV,  $\varepsilon_{Si}^s = -13.55$  eV,  $\varepsilon_{Si}^p = -6.52$  eV,  $\varepsilon_O^p = -14.13$  eV,  $\varepsilon_O^s = -29.14$  eV, and  $\varepsilon_{Mn}^d = -15.27$  eV.<sup>[73]</sup> The optimal values of tensile strain at 4% for nearest-neighbor are  $V_{ss\sigma} = -2.49$  eV,  $V_{sp\sigma} = 3.27$  eV,  $V_{pp\sigma} = 5.76$  eV,  $V_{pp\pi} = -1.44$  eV,  $V_{sd\sigma} = -6.42$  eV,  $V_{pd\pi} = 2.76$  eV,  $V_{pd\sigma} = -5.98$  eV, and  $V_{sd\pi} = 2.76$  eV, respectively. For the compression strain, the optimal values at -4% are calculated to  $V_{ss\sigma} = -1.40$  eV,  $V_{sp\sigma} = 4.09$  eV,  $V_{pp\sigma} = 7.21$  eV,  $V_{pp\pi} = -1.80$  eV,  $V_{sd\sigma} = -9.49$  eV,  $V_{pd\sigma} = -8.86$  eV, and  $V_{pd\pi} = 4.96$  eV.

Using Equation (3), we specifically analyzed the nearest-neighbor (Mn–O) on-site energy at  $\varepsilon = +4$  and at  $\varepsilon = -4\%$ .

When a biaxial tensile strain was applied to  $\text{Na}_2\text{MnSiO}_4$ , the lattice parameter expanded and the bond between atoms stretched, and the bandgap was lowered with increasing on-site energy. Biaxial compressive straining, on the other hand, resulting in a greater bandgap and decreased on-site energy (Figure 12 and Figures S3–S5, Supporting Information).

### Na<sup>+</sup>-Ion Diffusion in the Unstrained $\text{Na}_2\text{MnSiO}_4$ Structure

One of the important characteristics that determines the charge-discharge rate capabilities, and hence the electrochemical performance of rechargeable batteries, is conductivity (ionic, electronic, and/or polaronic). As in prior

investigations,<sup>[29,32,74]</sup> these parameters might be evaluated by manipulating Equations (1) and (2). The conductivity of the primary components of battery cells, such as electrodes (anode and cathode) and electrolytes, is used to choose them for use in battery applications. Before applying biaxial tensile strain (BTS), the Na<sup>+</sup>-ion conductivity in an unstrained monoclinic  $Pn$   $\text{Na}_2\text{MnSiO}_4$  crystal structure was investigated using the selected Na<sup>+</sup>-ion pathways and dimensionalities.

Figures 15 and 16 depict, respectively, the Na<sup>+</sup>-ion diffusion paths and the calculated activation energy barrier, that were used to calculate energy barriers ( $E_b$ ), diffusion rates ( $r$ ), and diffusion coefficients ( $D$ ). In the ZX-plane from E to A (EA), the X-axis from A to B (AB), the ZY-plane from A to C (AC), and the Y-axis from C to D (CD) were selected. Fast Na<sup>+</sup>-ion diffusion was observed along the Y(CD) channel with a diffusion coefficient of  $3.5 \times 10^{-5} \text{ cm}^2 \text{ s}^{-1}$  and a diffusion rate of  $3.14 \times 10^{10} \text{ s}^{-1}$ , due to the lowest energy barrier of 0.15 eV. The rising energy barrier for Na<sup>+</sup>-ion diffusion is in the following order: ZX(EA) > X(AB) > ZY(AC) > Y(CD), resulting into the slowest Na<sup>+</sup>-ion diffusion along the ZX(EA) channel.

Table S1 (Supporting Information) also summarizes the diffusion coefficients, diffusion rates, and activation energy barriers before and after applying biaxial strain. The calculated

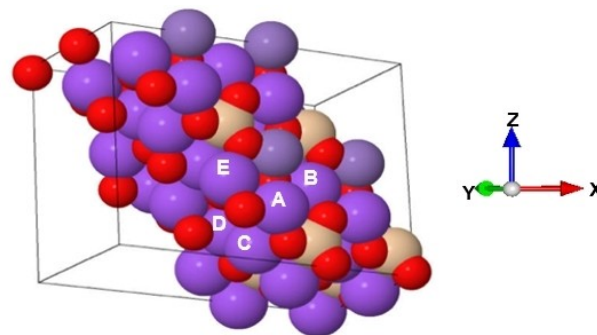


Figure 15. The crystal structure of  $\text{Na}_2\text{MnSiO}_4$  with a  $2 \times 2 \times 2$  supercell. The pink, gray, cyan, and red, respectively, represent Na, Mn, Si, and O atoms.

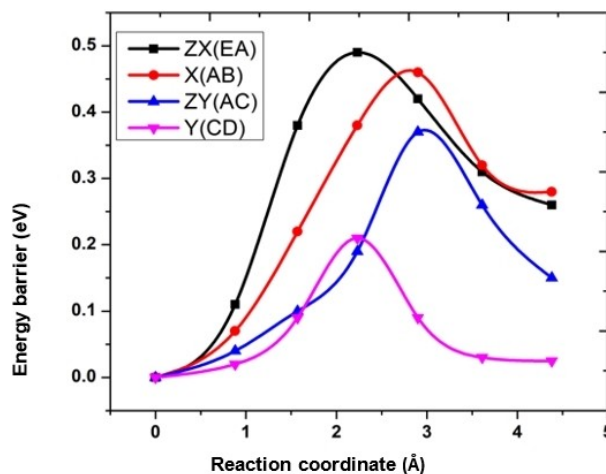


Figure 16. Energy barriers calculated by CI-NEB method for four Na<sup>+</sup>-ion diffusion pathways in unstrained  $\text{Na}_2\text{MnSiO}_4$  bulk structure.

energy barriers ( $E_b$ ) confirm the possibility of  $\text{Na}^+$ -ion conduction in the selected channels in agreement with previous DFT calculations results.<sup>[18,28,33]</sup>

This work also reveals better  $\text{Na}^+$ -ion diffusivity in Na-based orthosilicate than  $\text{Li}^+$ -ion conduction in Li-based orthosilicate compounds.<sup>[29,33]</sup> For instance, it was indicated that the ionic conduction of orthosilicate compounds is related to their constituent elements and crystal systems:  $\text{Na}_2\text{MnSiO}_4 > \text{NaLiMnSiO}_4 > \text{Li}_2\text{MnSiO}_4$ . The related channels get extended for higher  $\text{Na}^+$ -ion migration with less energy cost than Li-based systems as the volume of the Na-based compounds of the same system expands due to the atomic radius of Na metal.

### $\text{Na}^+$ -Ion Diffusion in the Biaxially Strained $\text{Na}_2\text{MnSiO}_4$ Structure

Superior sodium-ion diffusivity is of vital importance to enhancing the conductivity and thus realizing a higher rate performance of the battery. The biaxial strain was applied to the ZX-plane along the EA path (ZX(EA)) to study the Na-ion diffusion from A to E. The calculated energy barrier ( $E_b$ ) decreases from 0.54 to 0.36 eV as biaxial strain was applied from  $\epsilon = -4\%$  (BCS,  $\epsilon < 0$ ) to  $\epsilon = 4\%$  (BTS,  $\epsilon > 0$ ). The biaxial tensile strain (BTS) at  $\epsilon = 4\%$  and  $\epsilon = 2\%$ , as well as the biaxial compressive strain (BCS) at  $\epsilon = -4\%$  and  $\epsilon = -2\%$ , were applied to the bulk  $\text{Na}_2\text{MnSiO}_4$  crystal structure with greater energy barrier ( $E_b = 0.49$  eV) calculated along ZX (EA). In biaxially tensile-strained  $\text{Na}_2\text{MnSiO}_4$ , the diffusion of  $\text{Na}^+$ -ions is faster than for the biaxial compressive version, as shown in Figure 17 and Table S2 (Supporting Information). The calculated energy barriers as a function of biaxial strain along the ZX(EA) path have been estimated to 0.44 and 0.36 eV in BTS at  $\epsilon = +4\%$  and at  $\epsilon = +2\%$ , respectively. The corresponding faster rates and diffusion coefficients were estimated to  $3.62 \times 10^5 \text{ s}^{-1}$  ( $\epsilon = +2\%$ ),  $8.16 \times 10^6 \text{ s}^{-1}$  ( $\epsilon = +4\%$ ),  $3.82 \times 10^{-10} \text{ cm}^2 \text{ s}^{-1}$  ( $\epsilon = +2\%$ ) and  $8.6 \times 10^{-9} \text{ cm}^2 \text{ s}^{-1}$  ( $\epsilon = +4\%$ ), respectively. Results revealed the improvement of  $\text{Na}^+$ -ion diffusion rate and diffusion coefficient by two orders of magnitude compared to

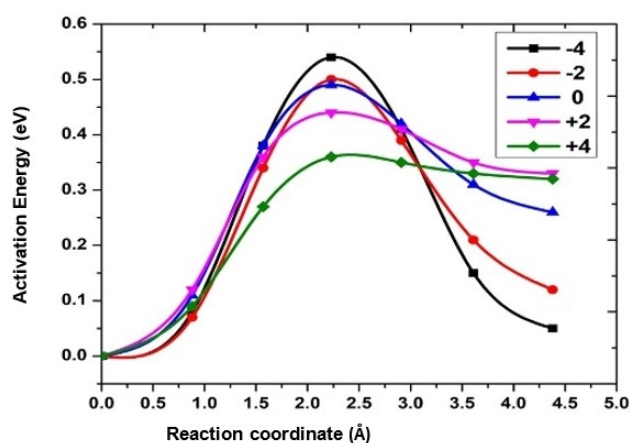


**Figure 17.** Energy barriers calculated by CI-NEB method for four  $\text{Na}^+$ -ion diffusion pathways as a function of biaxial lattice strain from  $\epsilon = -4$  to  $4\%$ .

unstrained  $Pc$   $\text{Na}_2\text{MnSiO}_4$  (at  $\epsilon = 0$ ). Therefore, it would make sense to have a look at the Na–O bond length for the initial configuration by removing the Na atom at E (Figure 15) and also for the final configuration by moving the Na atom from A and replacing it at E.

The Na–O ( $\text{NaO}_4$ ) bond lengths without straining ( $\epsilon = 0\%$ ) and after biaxial straining ( $\epsilon = -4, -2, 2$ , and  $4\%$ ) of initial and final configurations are summarized in Table S3 (Supporting Information). The average bond length Na–O is larger ( $2.538 \text{ \AA}$ ) in the initial configuration than that of the final configuration ( $2.436 \text{ \AA}$ ) without straining ( $\epsilon = 0\%$ ). This implies that the initial energy required to diffuse  $\text{Na}^+$ -ion is less than that of final energy, resulting in different initial and final energies. The considered paths follow the stability order from higher to lower:  $\text{Y(CD)} > \text{ZY(AC)} > \text{X(AB)} > \text{ZX(EA)}$ , resulting also in different initial and final energy states.

When biaxial straining was applied from  $\epsilon = -4$  to  $+4\%$ , the average bond length Na–O is monotonically increasing with respect to the applied biaxial strain from  $\epsilon = -4$  to  $2\%$  with bonding strength of  $2.450 \text{ \AA}$  ( $\epsilon = -4\%$ )  $>$   $2.530 \text{ \AA}$  ( $\epsilon = -2\%$ )  $>$   $2.660 \text{ \AA}$  ( $\epsilon = 2\%$ )  $>$   $2.74 \text{ \AA}$  ( $\epsilon = 4\%$ ) for the initial configuration and also  $2.360 \text{ \AA}$  ( $\epsilon = -4\%$ )  $>$   $2.371 \text{ \AA}$  ( $\epsilon = -2\%$ )  $>$   $2.499 \text{ \AA}$  ( $\epsilon = 2\%$ ) for the final configuration. In contrast, when biaxial tensile strain ( $\epsilon = 4\%$ ) was applied to the final configuration, the average bond length Na–O decreased to  $2.481 \text{ \AA}$ . Due to the ability of biaxial tensile straining to increase the average bond length Na–O, establishing stronger bonds with Mn ( $\text{MnO}_4$ ) and Si ( $\text{SiO}_4$ ) tetrahedral complexes would be easier and would need less energy. The bond length of Mn–O was found to vary whereas Si–O bonding regardless of the applied biaxial strain remain constant. For instance, the average Mn–O bond length increases with biaxial straining of  $\epsilon = -2\%$  ( $2.431 \text{ \AA}$ ) and  $\epsilon = 2\%$  ( $2.389 \text{ \AA}$ ), but decreases with that of  $\epsilon = -4\%$  ( $2.346 \text{ \AA}$ ) and  $\epsilon = 4\%$  ( $2.614 \text{ \AA}$ ).

In principle, compressing and elongating the average bond length Mn–O keeps the system symmetric by reducing the degeneracy caused by the Jahn-Teller distortion.<sup>[75]</sup> This Jahn-Teller distortion only affects local environments where Mn is surrounded by four O ( $\text{MnO}_4$  tetrahedral environment) or six O ( $\text{MnO}_6$  octahedral environment) atoms as summarized in Table S1 (Supporting Information). The bonding readjustment with reasonable range, with no significant impact on the lattice, would facilitate the  $\text{Na}^+$ -ion (de)intercalation from and/into  $\text{Na}_2\text{MnSiO}_4$  cathode during charging and/or discharging process in rechargeable Na-ion batteries. When it comes to the Si–O bond in  $\text{SiO}_4$  as a function of biaxial straining, the average bond formation tendency increases monotonically from  $\epsilon = -4\%$  to  $4\%$ , following the bond strength order:  $1.644 \text{ \AA}$  ( $\epsilon = -4\%$ )  $>$   $1.652 \text{ \AA}$  ( $\epsilon = -2\%$ )  $>$   $1.664 \text{ \AA}$  ( $\epsilon = 2\%$ )  $>$   $1.670 \text{ \AA}$  ( $\epsilon = 4\%$ ) for the initial configurations, and also  $1.587 \text{ \AA}$  ( $\epsilon = -4\%$ )  $>$   $1.651 \text{ \AA}$  ( $\epsilon = -2\%$ )  $>$   $1.663 \text{ \AA}$  ( $\epsilon = 2\%$ )  $>$   $1.668 \text{ \AA}$  ( $\epsilon = 4\%$ ) for the final configurations.

The final configuration has a significantly longer average bond length than that of the initial configuration, resulting in a relatively minor structural deformation that could raise up the energy of the final configuration. Therefore, it should be clear that applying biaxial tensile strain (BTS) is an effective method

to enhancing both the electronic transport and the rate performance of  $\text{Na}_2\text{MnSiO}_4$  material as a promising cathode electrode for rechargeable  $\text{Na}^+$ -ion batteries (SIBs).

Previous DFT results have also demonstrated the same trend in the case of  $\text{Li}^+$ -ion migration energy barrier under applied BTS on orthosilicate ( $\text{A}_2\text{MnSiO}_4$ ,  $\text{A}=\text{Li}, \text{Na}$ )<sup>[33,76]</sup> and for olivine systems ( $\text{AFePO}_4$ ,  $\text{A}=\text{Li}, \text{Na}$ )<sup>[77]</sup> for ionic migration. The DFT analysis revealed higher  $\text{Na}^+$ -ion diffusion rates and diffusion coefficients as a function of applied BTS in the orthosilicate family, as a promising strategy for alkali-ion diffusion in cathode materials for optimized electrochemical rate performance in rechargeable batteries. In this regard, we expect that the biaxially tensile-strained  $\text{Na}_2\text{MnSiO}_4$  crystal structure could be observed experimentally.

## Conclusion

DFT+U combined with AIMD and tight-binding model (TBM) analysis was used to investigate the structural stability, electronic and  $\text{Na}^+$ -ion conductivity in  $\text{Na}_2\text{MnSiO}_4$  before and after applying biaxial strain. Results revealed that the structural stability evolved with applied compressive/tensile strain of  $\varepsilon = -4\%$  to  $\varepsilon = +4\%$ . Analysis from the electronic projected density of states revealed strong orbitals coupling between O (2p) and Mn (3d), which are thus expected to be the main cause for electron transfer in  $\text{Na}_2\text{MnSiO}_4$  material. The calculated band structure also proved that the electronic bandgap is slightly wider for applied biaxial compressive strain ( $E_g = 2.64$  eV, at  $\varepsilon = -4\%$ ) than for biaxial tensile strain ( $E_g = 2.2$  eV, at  $\varepsilon = +4\%$ ). These results infer that the electronic density of states and band structures of  $\text{Na}_2\text{MnSiO}_4$  are sensitive to biaxial strain. Moreover,  $\text{Na}^+$ -ion diffusivity decreases with biaxial compressive strain ( $D = 7.77 \times 10^{-12} \text{ cm}^2 \text{ s}^{-1}$  at  $\varepsilon = -4\%$ ) while it increases with a biaxial tensile strain ( $D = 8.60 \times 10^{-9} \text{ cm}^2 \text{ s}^{-1}$  at  $\varepsilon = +4\%$ ). This study revealed that the rational biaxial tensile strain design in the  $\text{Na}_2\text{MnSiO}_4$  material remarkably lifts the electronic conductivity due to the induced narrow electronic bandgap. Furthermore, enhanced  $\text{Na}^+$ -ion diffusion channels were observed with the biaxial lattice tensile straining of  $\text{Na}_2\text{MnSiO}_4$ . In turn, it increases its volume, opening more vacant spaces in the system, and enabling a higher rate of  $\text{Na}^+$ -ion migration. Consequently, the results suggest that the appropriate biaxial tensile lattice strain engineering paves the way for a promising approach to design efficient electrode materials for sodium-based energy storage rechargeable battery devices.

## Acknowledgements

This work was supported by a thematic research project (Grant no. TR/036/2020) funded by Addis Ababa University. The authors would like to acknowledge the computational resource support from the Ethiopian Education and Research Network (EthERNET) at the Ethiopian Ministry of Science and Higher Education. Y. S. Mekonnen would like to thank the World Academy of Sciences (TWAS) for supporting this work (Grants No. 19-202 RG/CHE/AF/

AC\_G-FR3240310122). G. S. Gurmesa would like to acknowledge Mettu University for sponsorship. Ayan Datta thanks DST India for the research grant for computational resources vide DIA/2018/000013 and CRG/2020/000301.

## Conflict of Interest

The authors declare no conflict of interest.

## Data Availability Statement

The data that support the findings of this study are available in the supplementary material of this article.

**Keywords:** DFT · AIMD · biaxial lattice strain · diffusion · Na-ion battery ·  $\text{Na}_2\text{MnSiO}_4$

- [1] B. L. Ellis, L. F. Nazar, *Curr. Opin. Solid State Mater. Sci.* **2012**, *16*, 168–177.
- [2] V. Palomares, M. Casas-Cabanas, E. Castillo-Martinez, M. H. Han, T. Rojo, *Energy Environ. Sci.* **2013**, *6*, 2312–2337.
- [3] N. Yabuuchi, K. Kubota, M. Dahbi, S. Komaba, *Chem. Rev.* **2014**, *114*, 11636–11682.
- [4] H. Pan, Y. S. Hu, L. Chen, *Energy Environ. Sci.* **2013**, *6*, 2338–2360.
- [5] C. Zhao, Q. Wang, Z. Yao, J. Wang, F. Ding, X. Qi, Y. Lu, X. Bai, B. Li, H. Li, X. Huang, C. Delmas, M. Wagemaker, L. Chen, Y. Hu, *Science* **2020**, *711*, 708–711.
- [6] P. Wang, Y. You, Y. Yin, Y. Guo, *Adv. Energy Mater.* **2017**, *8*, 1701912.
- [7] W. Zuo, J. Qiu, X. Liu, F. Ren, H. Liu, H. He, C. Luo, J. Li, G. F. Ortiz, H. Duan, J. Liu, M. Wang, Y. Li, R. Fu, Y. Yang, *Nat. Commun.* **2020**, *11*, 3544.
- [8] D. D. MacNeil, Z. Lu, J. R. Dahn, *J. Electrochem. Soc.* **2002**, *149*, A1332.
- [9] N. Yabuuchi, T. Ohzuku, *J. Power Sources* **2003**, *119*, 171.
- [10] I. Belharouak, Y. K. Sun, J. Liu, K. Amine, *J. Power Sources* **2003**, *123*, 247–252.
- [11] K. M. Shaju, G. V. Subba Rao, B. V. R. Chowdari, *Electrochim. Acta* **2002**, *48*, 145–151.
- [12] B. Senthilkumar, K. V. Sankar, L. Vasylechko, Y. S. Lee, R. K. Selvan, *RSC Adv.* **2014**, *4*, 53192–53200.
- [13] F. Bianchini, H. Fjellvåg, P. Vajeeston, *Mater. Chem. Phys.* **2018**, *219*, 212–221.
- [14] G. Xu, K. Zhong, J. M. Zhang, Z. Huang, *J. Appl. Phys.* **2014**, *116*, 063703.
- [15] A. V. Churikov, A. V. Ivanishchev, I. A. Ivanishcheva, V. O. Sycheva, N. R. Khasanova, E. V. Antipov, *Electrochim. Acta* **2010**, *55*, 2939–2950.
- [16] G. K. P. Dathar, D. Sheppard, K. J. Stevenson, G. Henkelman, *Chem. Mater.* **2011**, *23*, 4032.
- [17] H. N. Girish, G. Q. Shao, *RSC Adv.* **2015**, *5*, 98666.
- [18] F. Bianchini, H. Fjellvåg, P. Vajeeston, *Phys. Chem. Chem. Phys.* **2017**, *19*, 14462–14470.
- [19] Y. Wei, Y. Huang, Y. Zhang, J. Ding, X. Wang, W. Cheng, Y. Sun, D. Jia, X. Tang, *Energy Reports* **2020**, *6*, 2191–2199.
- [20] R. Dominko, M. Bele, A. Kokalj, M. Gaberscek, J. Jamnik, *J. Power Sources* **2007**, *174*, 457.
- [21] Y. Zhang, H. Zhou, *J. Mater. Chem. A* **2014**, *2*, 11574–11577.
- [22] C. Masquelier, L. Croguennec, *Chem. Rev.* **2013**, *113*, 6552–6591.
- [23] P. Barpanda, G. Oyama, S. I. Nishimura, S. C. Chung, A. Yamada, *Nat. Commun.* **2014**, *5*, 4358.
- [24] M. Law, V. Ramar, P. Balaya, *J. Power Sources* **2017**, *359*, 277–284.
- [25] H. Zhu, J. Wang, X. Liu, X. Zhu, *RSC Adv.* **2017**, *7*, 14145–14151.
- [26] C. Y. Chen, K. Matsumoto, T. Nohira, R. Hagiwara, *Electrochem. Commun.* **2014**, *45*, 63–66.
- [27] J. C. Treacher, S. M. Wood, M. S. Islam, E. Kendrick, *Phys. Chem. Chem. Phys.* **2016**, *18*, 32744–32752.
- [28] N. Kuganathan, A. Chronos, *Sci. Rep.* **2018**, *8*, 5–11.
- [29] G. S. Gurmesa, N. E. Benti, M. D. Chaka, G. A. Tiruye, Q. Zhang, Y. S. Mekonnen, C. A. Geffe, *RSC Adv.* **2021**, *11*, 9721–9730.

- [30] W. B. Begna, G. S. Gurmesa, Q. Zhang, C. A. Geffe, *AIP Adv.* **2022**, *12*, 025002.
- [31] G. Shiferaw Aga, G. S. Gurmesa, Q. Zhang, P. Singh, C. A. Geffe, *Comput. Condens. Matter* **2022**, *30*, e00628.
- [32] Y. S. Mekonnen, J. M. Garcia-Lastra, J. S. Hummelshøj, C. Jin, T. Vegge, *J. Phys. Chem. C* **2015**, *119*, 18066–18073.
- [33] P. Zhang, Y. Xu, F. Zheng, S. Q. Wu, Y. Yang, Z. Z. Zhu, *CrystEngComm* **2015**, *17*, 2123–2128.
- [34] A. R. Armstrong, C. Sirisopanaporn, P. Adamson, J. Billaud, R. Dominko, C. Masquelier, P. G. Bruce, *Z. Anorg. Allg. Chem.* **2014**, *640*, 1043.
- [35] S. Q. Wu, Z. Z. Zhu, Y. Yang, Z. F. Hou, *Comput. Mater. Sci.* **2009**, *44*, 1243.
- [36] C. Sirisopanaporn, R. Dominko, C. Masquelier, A. R. Armstrong, G. Mali, P. G. Bruce, *J. Mater. Chem.* **2011**, *21*, 17823.
- [37] V. B. Nalbandyan, E. A. Zvereva, I. L. Shukaev, E. Gordon, V. V. Politaev, M. H. Whangbo, A. A. Petrenko, R. S. Denisov, M. M. Markina, M. Tschoppe, K. Y. Bukhteev, R. Klingeler, A. N. Vasiliev, *Inorg. Chem.* **2017**, *56*, 14023–14039.
- [38] A. Jain, S. P. Ong, G. Hautier, W. Chen, W. D. Richards, S. Dacek, S. Cholia, D. Gunter, D. Skinner, G. Ceder, K. A. Persson, *APL Mater.* **2013**, *1*, 011002.
- [39] P. Chaturvedi, A. Sil, Y. Sharma, *Solid State Ionics* **2016**, *297*, 68.
- [40] T. Muraliganth, K. R. Stroukoff, A. Manthiram, *Chem. Mater.* **2010**, *22*, 5754.
- [41] P. Babbar, B. Tiwari, B. Purohit, A. Ivanishchev, A. Churikov, A. Dixit, *RSC Adv.* **2017**, *7*, 22990.
- [42] Q. Ni, Y. Bai, F. Wu, C. Wu, *Adv. Sci.* **2017**, *4*, 1600275.
- [43] J. Chen, *Materials* **2013**, *6*, 156–183.
- [44] X. Sun, R. Tripathi, G. Popov, M. Balasubramanian, L. F. Nazar, *Inorg. Chem.* **2017**, *56*, 9931–9937.
- [45] T. Jin, H. Li, K. Zhu, P. F. Wang, P. Liu, L. Jiao, *Chem. Soc. Rev.* **2020**, *49*, 2342–2377.
- [46] M. S. Islam, R. Dominko, C. Masquelier, C. Sirisopanaporn, A. R. Armstrong, P. G. Bruce, *J. Mater. Chem.* **2011**, *21*, 9811.
- [47] M. Ernzerhof, G. E. Scuseria, *Theor. Chem. Acc.* **2000**, *103*, 259.
- [48] W. Kohn, J. Sham, *Phys. Rev. B* **1965**, *140*, A 1133.
- [49] J. Enkovaara, C. Rostgaard, J. J. Mortensen, J. Chen, M. Dulak, L. Ferrighi, J. Gavnholt, C. Glinsvad, V. Haikola, H. A. Hansen, H. H. Kristoffersen, M. Kuisma, A. H. Larsen, L. Lehtovaara, M. Ljungberg, O. Lopez-Acevedo, P. G. Moses, J. Ojanen, T. Olsen, V. Petzold, N. A. Romero, J. Stausholm-Møller, M. Strange, G. A. Tritsarlis, M. Vanin, M. Walter, B. Hammer, H. Häkkinen, G. K. H. Madsen, R. M. Nieminen, J. K. Nørskov, M. Puska, T. T. Rantala, J. Schiøtz, K. S. Thygesen, K. W. Jacobsen, *J. Phys. Condens. Matter* **2010**, *22*, 253202.
- [50] J. Hafner, G. Kresse, The Vienna AB-Initio Simulation Program VASP: An Efficient and Versatile Tool for Studying the Structural, Dynamic, and Electronic Properties of Materials. In *Properties of Complex Inorganic Solids*, A. Gonis, A. Meike, P. E. A. Turchi, Eds., Springer, Boston, 1997, 69–82.
- [51] J. P. Perdew, K. Burke, M. Ernzerhof, *Phys. Rev. Lett.* **1996**, *77*, 3865–3868.
- [52] P. E. Blochl, *Phys. Rev. B* **1994**, *50*, 17953.
- [53] S. L. Dudarev, G. A. Botton, S. Y. Savrasov, C. J. Humphreys, A. P. Sutton, *Phys. Rev. B* **1998**, *57*, 1505–1509.
- [54] V. I. Anisimov, J. Zaanen, O. K. Andersen, *Phys. Rev. B* **1991**, *44*, 943–954.
- [55] T. Teshome, A. Datta, *ACS Omega* **2018**, *3*, 1–7.
- [56] T. Teshome, A. Datta, *ACS Appl. Mater. Interfaces* **2017**, *9*, 34213–34220.
- [57] T. Teshome, A. Datta, *J. Phys. Chem. C* **2018**, *122*, 25127–25133.
- [58] G. Henkelman, H. Jónsson, *J. Chem. Phys.* **2000**, *113*, 9978.
- [59] P. Hänggi, P. Talkner, M. Borkovec, *Rev. Mod. Phys.* **1990**, *62*, 251–341.
- [60] T. Vegge, T. Rasmussen, T. Leffers, O. B. Pedersen, K. W. Jacobsen, *Phys. Rev. Lett.* **2000**, *85*, 3866–3869.
- [61] O. C. Gagné, F. C. Hawthorne, *Acta Crystallogr. Sect. B* **2017**, *73*, 1019–1031.
- [62] S. V. Sukhominov, M. H. Müser, *J. Chem. Phys.* **2017**, *146*, 024506.
- [63] A. Tandia, *J. Non-Cryst. Solids* **1997**, *216*, 14–18.
- [64] H. Ohsaki, K. Miura, *J. Sol-Gel Sci. Technol.* **1994**, *2*, 245–249.
- [65] K. Trabelsi, K. Karoui, A. Mahmoud, J. Bodart, F. Boschini, A. B. Rhaïem, *RSC Adv.* **2020**, *10*, 27456–27473.
- [66] R. Dominko, *J. Power Sources* **2008**, *184*, 462.
- [67] S. Li, J. Guo, Z. Ye, X. Zhao, S. Wu, J. X. Mi, C. Z. Wang, Z. Gong, M. J. McDonald, Z. Zhu, K. M. Ho, Y. Yang, *ACS Appl. Mater. Interfaces* **2016**, *8*, 17233–17238.
- [68] Y. Kawabe, N. Yabuuchi, M. Kajiyama, N. Fukuhara, T. Inamasu, R. Okuyama, I. Nakai, S. Komaba, *Electrochem. Commun.* **2011**, *13*, 1225–1228.
- [69] A. Kokalj, R. Dominko, G. Mali, A. Meden, M. Gaberscek, J. Jamnik, *Chem. Mater.* **2007**, *19*, 3633.
- [70] P. Vajeeston, F. Bianchini, H. Fjellvåg, *Energies* **2019**, *12*, 224.
- [71] N. A. Chernova, G. M. Nolis, F. O. Omenya, H. Zhou, Z. Li, M. S. Whittingham, *J. Mater. Chem.* **2011**, *21*, 9865–9875.
- [72] A. J. Ilott, M. Mohammadi, C. M. Schauermaier, M. J. Ganter, A. Jerschow, *Nat. Commun.* **2018**, *9*, 1776.
- [73] P. Vogl, H. P. Hjalmarson, J. D. Dow, *J. Phys. Chem. Solids* **1983**, *44*, 365–378.
- [74] N. E. Benti, G. S. Gurmesa, C. A. Geffe, A. M. Mohammed, G. A. Tiruye, Y. S. Mekonnen, *J. Mater. Chem. A* **2022**, *10*, 8501–8514.
- [75] Y. Liu, C. Wang, S. Zhao, J. Chen, L. Zhang, K. Zhang, F. Li, *Chem. Sci.* **2021**, *12*, 1062–1067.
- [76] M. Jia, H. Wang, Z. Sun, Y. Chen, C. Guo, L. Gan, *RSC Adv.* **2017**, *7*, 26089–26096.
- [77] C. Tealdi, J. Heath, M. S. Islam, *J. Mater. Chem. A* **2016**, *4*, 6998–7004.

Manuscript received: December 17, 2021  
Revised manuscript received: May 10, 2022